

ULRR

Design rules for antibody delivery by self-assembled block-copolyelectrolyte nanocapsules

Item Type	Article
Authors	Javan Nikkhah, Sousa;Cazade, Pierre-Andre;McManus, Jennifer J.;Thompson, Damien
Citation	Macromolecules 2022, 55, (7), pp. 2383–2397
Publisher	American Chemical Society
Download date	2026-06-16 05:43:56
Item License	https://creativecommons.org/licenses/by-nc-sa/4.0/
Link to Item	https://doi.org/10.34961/researchrepository-ul.24746040

Design rules for antibody delivery by self-assembled block-copolyelectrolyte nanocapsules

Sousa Javan Nikkhah §*, Pierre A. Cazade §, Jennifer J. McManus †, Damien Thompson §*

§ Department of Physics, Bernal Institute, University of Limerick, V94 T9PX Limerick, Ireland

† H. H Wills Physics Laboratory, University of Bristol, Bristol BS8 1TL, United Kingdom

Supporting Note 1: Current state of the art in experiments and modelling of protein encapsulation by organic self-assemblies

Xie *et al.*¹ very recently synthesized antibody fragment (Fab) carrying micelles comprised of cationic disulfide cross-linked poly(ethylene glycol) (PEG)-poly(L-lysine) block copolymers labeled with glucose transporter molecules to treat Alzheimer's disease by inhibiting aggregation of amyloid-beta (Ab) peptides in the brain parenchyma. Using the polymeric nanomicelle system they achieved the higher Fab accumulation in the brain compared to free Fab. Another system by Min *et al.*² also targeted brain parenchyma but instead demonstrated the encapsulation and delivery of antisense oligonucleotides (ASO) across the blood-brain barrier (BBB), using a polyion complex micelle self-assembled via electrostatic interactions from modified PEG-poly(L-lysine) copolymers. In this system, the ASO was captured in the core of the micelle with a dense shell of PEG, prolonging its circulation in blood. Li *et al.*³ designed a series of folate-functionalized PEG-L-glutamate derivatives as tumor-targeting carriers for cytochrome c (a positively charged protein), which showed improved drug-loading stability and protection of encapsulated proteins from degradation. Finally, Nukolova *et al.*⁴ developed a tumor-targeting mAb delivery platform based on diblock co-polyelectrolytes of PEG-poly(methacrylic acid) derivatives. Their novel surface-functionalized cross-linked nanogels represented highly swollen spherical polyelectrolyte particles with

free terminal aldehyde functionalities at the non-ionic PEG chains covalently conjugated to the amino groups of mAb.

Kim *et al.*⁵ created a polyion complex micelle structure loaded with mAb derivatives that were charge-converted to improve stability, delivery to the cytosol, and precise antigen recognition inside cells. Applying a mixture of homo- and block polycations in an appropriate ratio to construct polyion complex micelles significantly enhanced the endosomal escaping efficacy of the loaded antibody, leading to better recognition of intracellular antigens. Pispas *et al.*^{6,7} showed experimentally that complexation of lysozyme with sodium poly(sulfamate-carboxylate) isoprene-*block*-poly(ethylene oxide) (PSCI-*b*-PEO) anionic/neutral block copolymers results in micelle formation at neutral pH and in the salt concentration range of 0.05–0.15 M. They revealed that micellar structure and stability depended on the charge mixing ratio and the composition of the block copolymer. All these studies, however, have focused on experimentally observing polyions/protein and devising strategies to produce complex micelles without focusing on understanding the molecular mechanisms that drive the block co-polyelectrolyte/protein complex micelle formation. Understanding how polyion/protein complex micelles form is crucial for developing this unique protein delivery platform. However, due to the short time and length scales at which polyion/protein complex micelle form and operate, which are challenging to detect by experiments alone, there is still a lack of knowledge about the complex formation processes underlying protein transport.^{8,9} Suitably benchmarked and parameterized computer simulation methods can provide the necessary molecular details to better understand how the protein is encapsulated and transported by polyion complex micelle carriers. Molecular dynamics (MD) simulations have been recently used to understand the polyion/protein complex micelle formation. Using MD simulations, Zhang *et al.*¹⁰ showed that the micellization between lysozyme and PEG-poly(methacrylic acid) progressed via a two-step mechanism: (1) an electrostatically-driven adsorption of the poly(methacrylic acid) PMAA block onto the oppositely charged sites on lysozyme, and (2) the compaction of the complex driven by attractive hydrophobic interactions between non-polar lysozyme regions and the backbone of the PMAA.

Supporting Note 2: Coarse-grained force field

The dynamics of each particle (with index i) is governed by Newton's second law as follows

$$\frac{dr_i}{dt} = v_i, \quad \frac{dv_i}{dt} = f_i \quad (1)$$

Here, f_i represents the net force acting on a particle i and r_i, v_i represent the position vector and the velocity of the bead center of mass, respectively. f_i can be expressed as a combination of interparticle forces, *i.e.*, conservative force (F_{ij}^C), dissipative force (F_{ij}^D) and a random force (F_{ij}^R)¹¹ in the following form

$$f_i = \sum_{j \neq i} (F_{ij}^C + F_{ij}^D + F_{ij}^R) \quad (2)$$

The conservative force is a soft repulsive force acting between the particles as follows

$$F_{ij}^C = \begin{cases} a_{ij}(1 - r_{ij})\hat{r}_{ij} & (r_{ij} < r_c) \\ 0 & (r_{ij} \geq r_c) \end{cases} \quad (3)$$

Here, r_{ij} is the interparticle distance, \hat{r}_{ij} is the unit vector connecting the particles, and r_c is the cutoff distance. a_{ij} is the maximum interparticle repulsion which is often referred to as the interaction parameter. Additionally, the dissipative and random forces, which represent the collision between atoms, are coupled in a way that keeps the temperature constant and are given by

$$F_{ij}^D = -\gamma w^D(r_{ij})(\hat{r}_{ij} \cdot v_{ij})\hat{r}_{ij}, \quad F_{ij}^R = \sigma w^R(r_{ij})\theta_{ij}\hat{r}_{ij} \quad (4)$$

Here, $v_{ij} = v_i - v_j$, and w^D and w^R are weight functions associated with the dissipation and random forces, which obey the relation

$$w^D(r_{ij}) = [w^R(r_{ij})]^2 = \begin{cases} (1 - r_{ij})^2 & (r_{ij} < r_c) \\ 0 & (r_{ij} \geq r_c) \end{cases} \quad (5)$$

$\theta_{ij}(\mathbf{t})$ is a randomly fluctuating variable which satisfies, $\langle \theta_{ij}(\mathbf{t}) \rangle = 0$ and $\langle \theta_{ij}(\mathbf{t})\theta_{kl}(\mathbf{t}') \rangle = (\theta_{ik}\theta_{jl} + \theta_{il}\theta_{jk})\delta(\mathbf{t} - \mathbf{t}')$, where $\delta(\mathbf{t})$ is the delta function. σ and γ represent the amplitude of the random and the dissipative forces and are coupled by $\sigma^2 = 2\gamma k_B T$, where

k_B is the Boltzmann constant, and T is the temperature of the system. In our simulations, γ is chosen as 4.5¹¹ and $k_B T$ is chosen as 1.0.¹²

Groot and Warren¹¹ mapped the DPD model onto the Flory–Huggins (FH) model and established a link between \mathbf{a}_{ij} and the chi-parameter χ_{ij} :

$$\chi_{ij} = 2C\rho r_c^3 \left(\mathbf{a}_{ij} - \frac{\mathbf{a}_{ii} + \mathbf{a}_{jj}}{2} \right) \frac{r_c}{k_B T} \quad (6)$$

where ρ is the total particle density and C is a constant that depends on ρ . Assuming $\mathbf{a}_{ii} = \mathbf{a}_{jj}$ and using the equation of state for the soft repulsive DPD fluid together with the compressibility value for ambient water, Groot and Warren derived an expression for like-repulsive parameters:

$$\frac{\mathbf{a}_{ii} r_c}{k_B T} = \frac{\mathbf{a}_{jj} r_c}{k_B T} = \frac{75}{\rho r_c^3} \quad (7)$$

They further obtained linear relationships between \mathbf{a}_{ij} and χ_{ij} for $\rho = 3$:

$$\frac{\mathbf{a}_{ij} r_c}{k_B T} = \frac{\mathbf{a}_{ii} r_c}{k_B T} + 3.27 \chi_{ij} \quad (8)$$

For readers' comfort, we recall that the value $\mathbf{a}_{ij} = 25$ describes the favorable interaction and corresponds to $\chi_{ij} = 0$, $\mathbf{a}_{ij} = 26.64$ emulates the θ -state ($\chi_{ij} = 1/2$), while $\mathbf{a}_{ij} = 35$ describes a relatively unfavorable interaction corresponding to $\chi_{ij} \cong 3$, and $\mathbf{a}_{ij} = 40$ describes highly unfavorable interactions corresponding to $\chi_{ij} = 4.59$.

Electrostatic interactions

The motions of the uncharged beads are entirely governed by the coarse-grained force field described above; however, for charged beads, electrostatic interactions need to be carefully accounted for as well. In DPD method, the conservative force is well defined at $r_{ij} = 0$, with full overlap between particles. However, the electrostatic energy of two point charges diverges at $r_{ij} = 0$, and so the addition of the electrostatic interactions could result in unphysical collapse of oppositely charged beads on top of one another.¹³ To overcome this artefact, Groot¹³ proposed the use of charge distributions instead of point charges. In this context, González-Melchor et al.¹⁴ proposed to use the Ewald method in combination with charge distributions on DPD particles.

Accordingly, the Slater-type exponential distribution, $f(r) = \frac{q}{\pi\lambda^3} \exp(-\frac{2r}{\lambda})$ was used to describe the charge distribution in the beads in order to remove the divergence at $r_{ij} = 0$. Therefore, the electrostatic force between beads i and j is represented as

$$F_{ij}^E = \frac{q_i q_j}{4\pi r_{ij}^2} \lambda_B [1 - \exp(-2\beta r_{ij}) (1 + 2\beta r_{ij} (1 + \beta r_{ij}))] \hat{\mathbf{r}}_{ij} \quad (9)$$

Here, $\lambda_B = e^2 / (k_B T \epsilon_0 \epsilon_r R_c)$, where e is the elementary charge, ϵ_0 is the vacuum permittivity, ϵ_r is the relative permittivity of the medium, q is the charge, and $\beta = r_c / \lambda$ where λ is the decay length of charge. We used the decay length of the charge $\lambda = 0.2$ and Bjerrum length $\lambda_B = 1.1$ in DPD units. The long-range electrostatic interactions were calculated using the Ewald sum with cut-off $r_c^{el} = 3$, real-space convergence parameter $\alpha^{ES} = 0.975$ and reciprocal vector range $\mathbf{n}_{max} = (5, 5, 5)$.¹⁵

Bonded interactions

Bonded interactions include the bond potential, angle potential, and dihedral potential. The following standard expressions were used:

$$E_{bond} = k_{bond} (r_{ij} - r_{eq})^2 \quad (10)$$

$$E_{angle} = k_{angle} (\theta - \theta_{eq})^2 \quad (11)$$

$$E_{dihedral} = k_{dihedral} (1 + \cos(\varphi - \varphi_{eq})) \quad (12)$$

Here, E_{bond} , E_{angle} , and $E_{dihedral}$ represent the bond, angle, and dihedral potentials, respectively. k_{bond} , k_{angle} , and $k_{dihedral}$ represent the spring stiffness, while r_{eq} , θ_{eq} , and φ_{eq} denote the equilibrium bond length, angle, and dihedral terms, respectively. Here, the spring stiffness and the equilibrium values for the potential protein terms were taken from data available in the literature.^{16,17}

The polymer chains were modelled as fully flexible strings of repulsive beads (of the same size as the solvent beads), which are kept together by harmonic spring potentials. A value of k_{bond} between 2 and $4 \frac{k_B T}{r_c^2}$ and $r_{eq} = 0$ are typically utilized.^{11,13,15} In this study, we used the same k_{bond} value of 4 for the polyelectrolyte blocks. The neutral block of PEG was modelled by a linear chain consisting of coarse-grained monomers. The beads of PEG polymers are sequentially connected by a harmonic bond potential, with spring stiffness $k_{bond} = 2111.3 k_B T / r_c^2$ and equilibrium distance $r_{eq} = 0.4125 r_c$.¹⁸

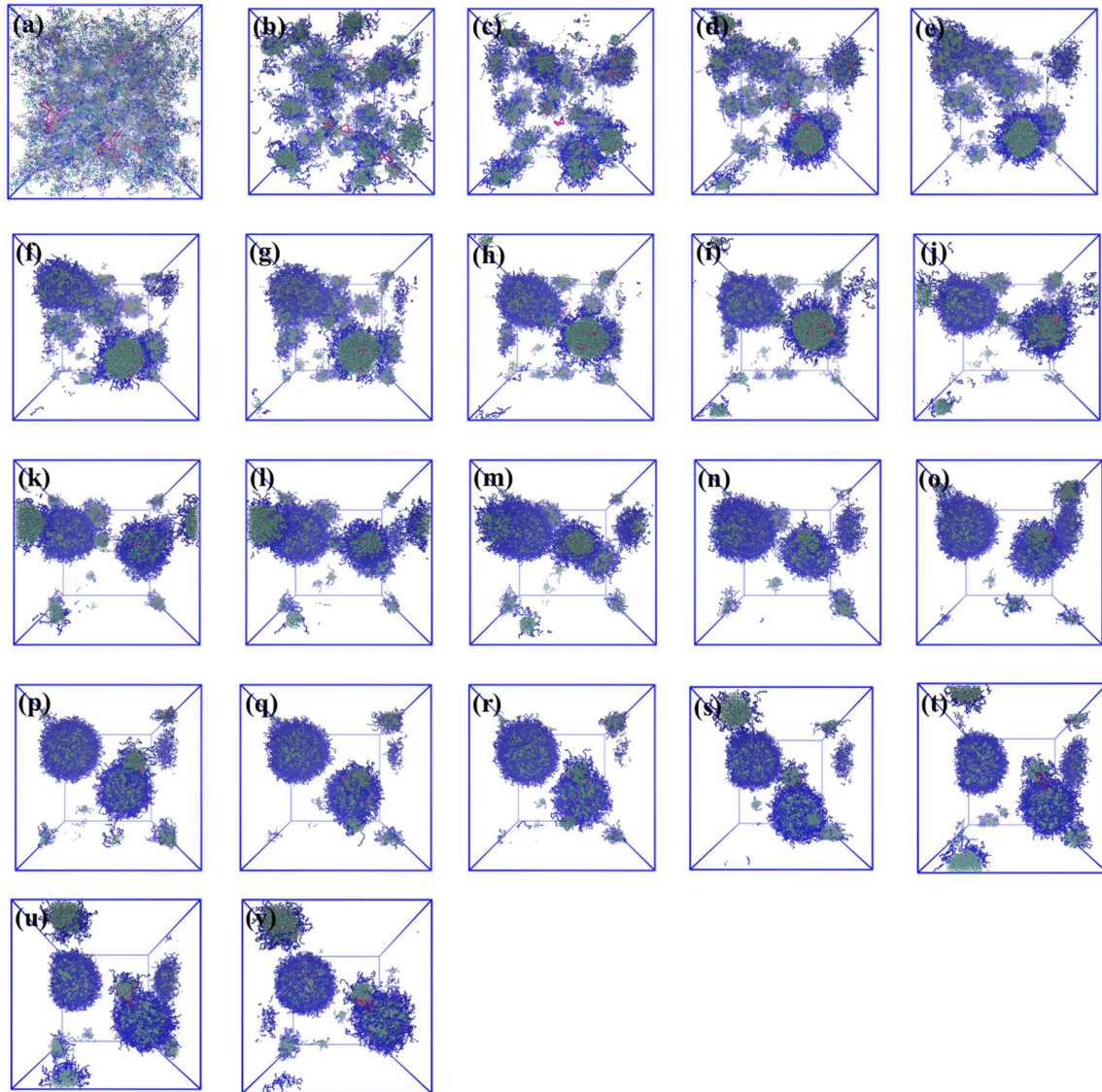


Figure S1. Time evolution of the aggregate formation and the final assembly morphology in the system consisting of IgG1, $A_{50}^+B_{30}$ and $A_{50}^-B_{30}$ ($l_t = 80, r_p = 0.60, \varphi_p = 0.05, a_{AW} = 40$). The snapshots correspond to simulation times (a) zero, (b) 3×10^4 , (c) 6×10^4 , (d) 9×10^4 , (e) 12×10^4 , (f) 15×10^4 , (g) 18×10^4 , (h) 24×10^4 , (i) 3×10^5 , (j) 3.6×10^5 , (k) 4.2×10^5 , (l) 4.8×10^5 , (m) 5.4×10^5 , (n) 6.0×10^5 , (o) 9.0×10^5 , (p) 1.2×10^6 , (q) 1.38×10^6 , (r) 1.5×10^6 , (s) 1.8×10^6 , (t) 2.4×10^6 , (u) 2.7×10^6 , and (v) 3×10^6 . Gray, cyan, blue and magenta beads represent A^- , A^+ , PEG, and IgG, respectively. Solvent and counterions are omitted in the visualizations for clarity.

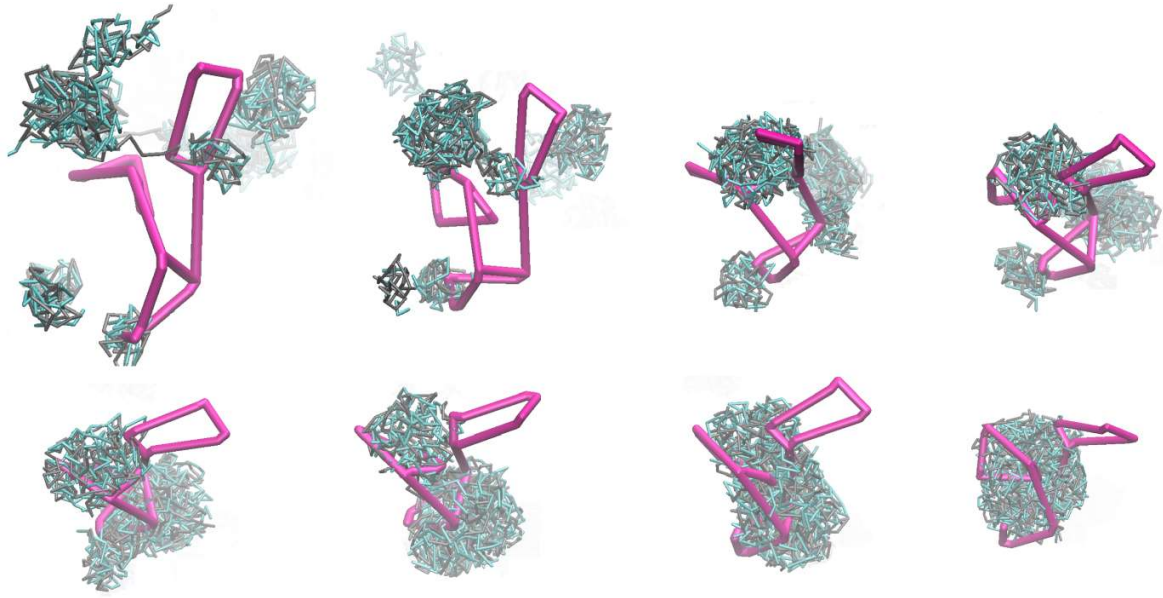


Figure S2. Visualisation of enveloping of IgG1. Magenta, cyan, and gray beads indicate IgG, A^- and A^+ , respectively. PEG beads are omitted in the visualizations for clarity.

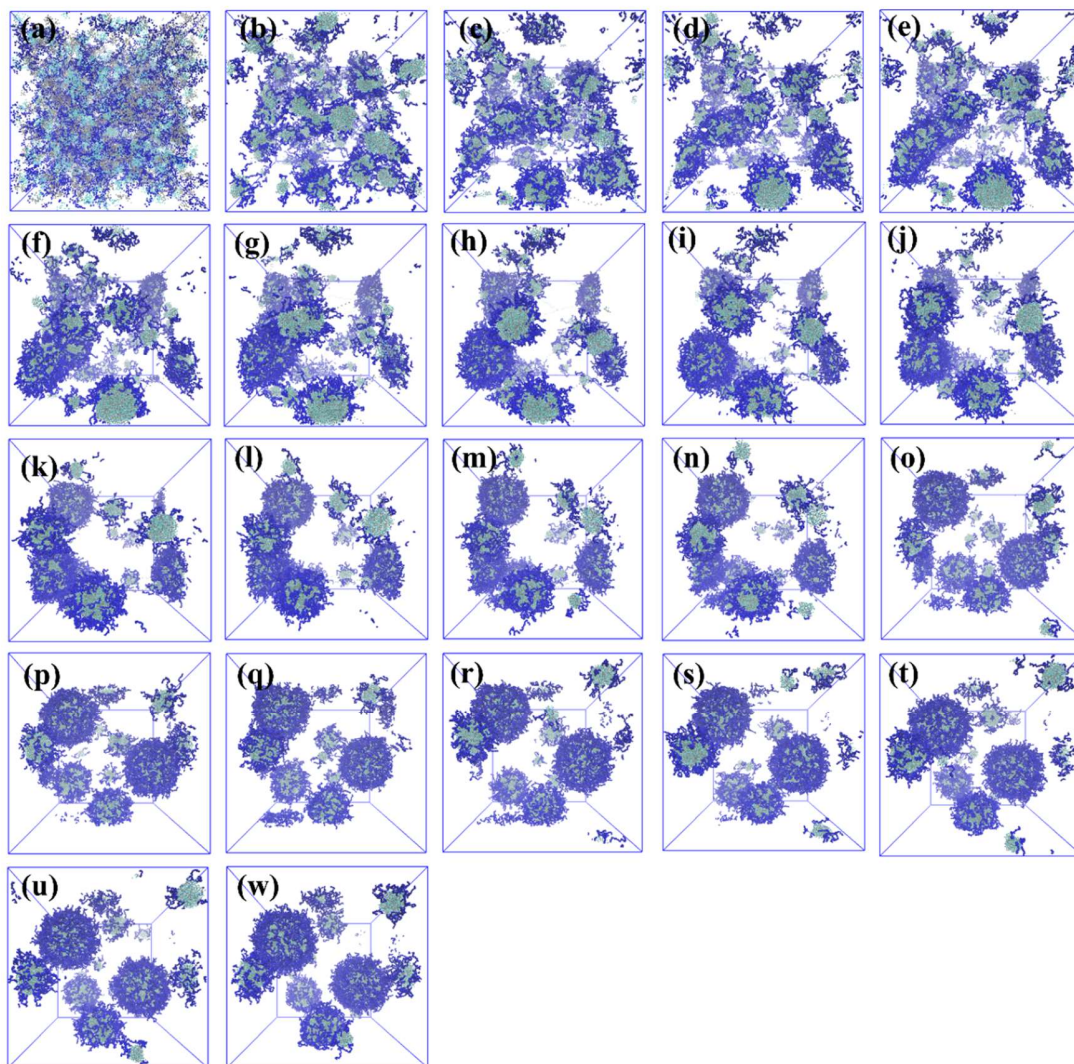


Figure S3. Time evolution of the aggregate formation and the final assembly morphology in the system consisting of $A_{50}^+B_{30}$ and $A_{50}^-B_{30}$ ($l_t = 80, r_b = 0.60, \varphi_p = 0.05, a_{AW} = 40$). The snapshots correspond to simulation times **(a)** zero, **(b)** 3×10^4 , **(c)** 6×10^4 , **(d)** 9×10^4 , **(e)** 12×10^4 , **(f)** 15×10^4 , **(g)** 18×10^4 , **(h)** 24×10^4 , **(i)** 3×10^5 , **(j)** 3.6×10^5 , **(k)** 4.2×10^5 , **(l)** 4.8×10^5 , **(m)** 5.4×10^5 , **(n)** 6.0×10^5 , **(o)** 9.0×10^5 , **(p)** 1.2×10^6 , **(q)** 1.38×10^6 , **(r)** 1.5×10^6 , **(s)** 1.8×10^6 , **(t)** 2.4×10^6 , **(u)** 2.7×10^6 , and **(v)** 3×10^6 . Gray, cyan, and blue beads represent A^- , A^+ , and PEG, respectively. Solvent and counterions are omitted in the visualizations for clarity.

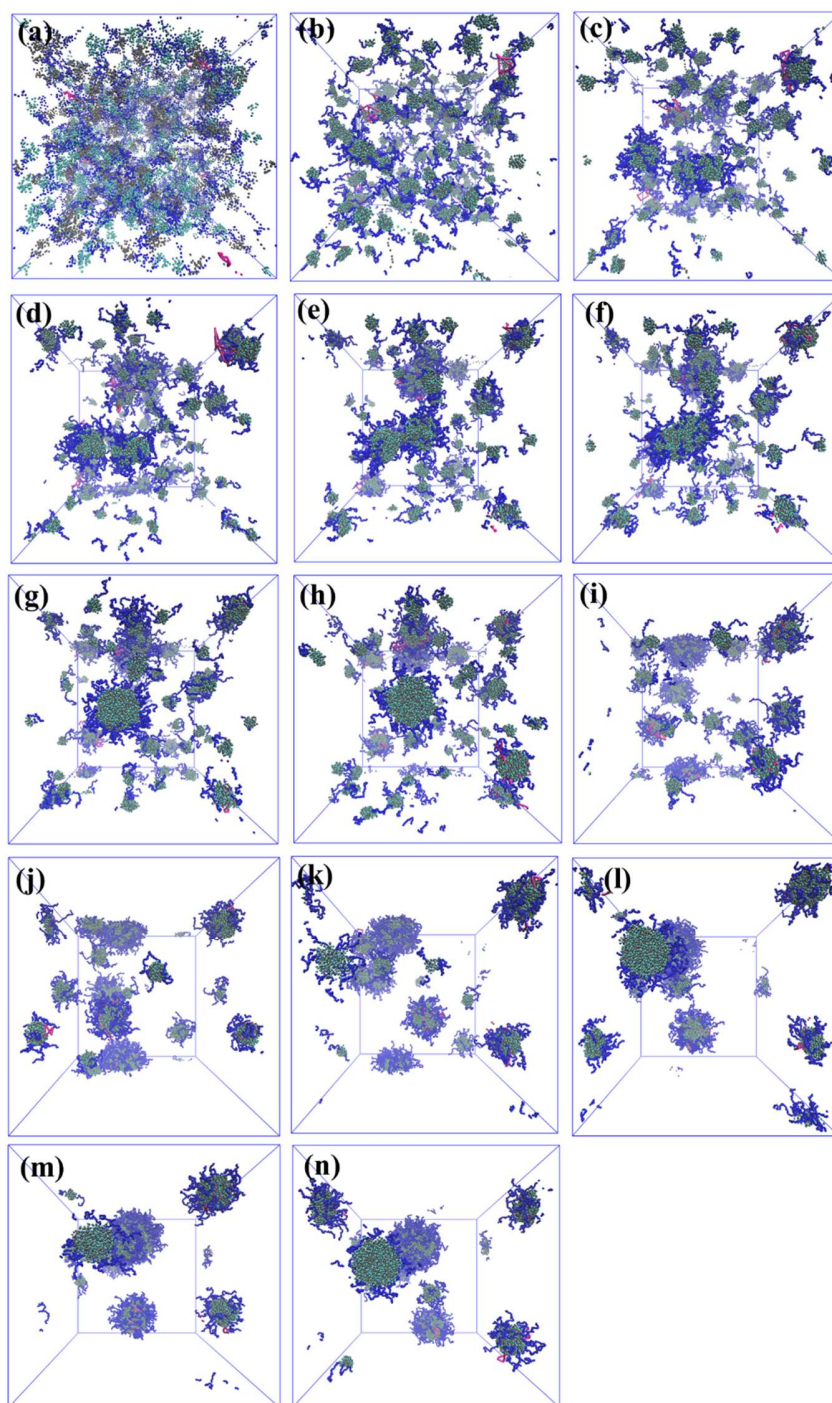


Figure S4. Time evolution of the aggregate formation and the final assembly morphology in the system consisting of IgG1, $A_{50}^+B_{30}$ and $A_{50}^-B_{30}$ ($l_t = 80$, $r_b = 0.60$, $\varphi_p = 0.02$, $a_{AW} = 40$). The snapshots correspond to simulation times (a) zero, (b) 1.2×10^4 , (c) 1.8×10^4 , (d) 6.0×10^4 , (e) 9.0×10^4 , (f) 9.6×10^4 , (g) 1.08×10^5 , (h) 1.8×10^5 , (i) 6.0×10^5 , (j) 1.2×10^6 , (k) 1.8×10^6 , (l) 2.4×10^6 , (m) 2.7×10^6 , and (n) 3.3×10^6 . Gray, cyan, blue and magenta beads represent A^- , A^+ , PEG, and IgG, respectively. Solvent and counterions are omitted in the visualizations for clarity.

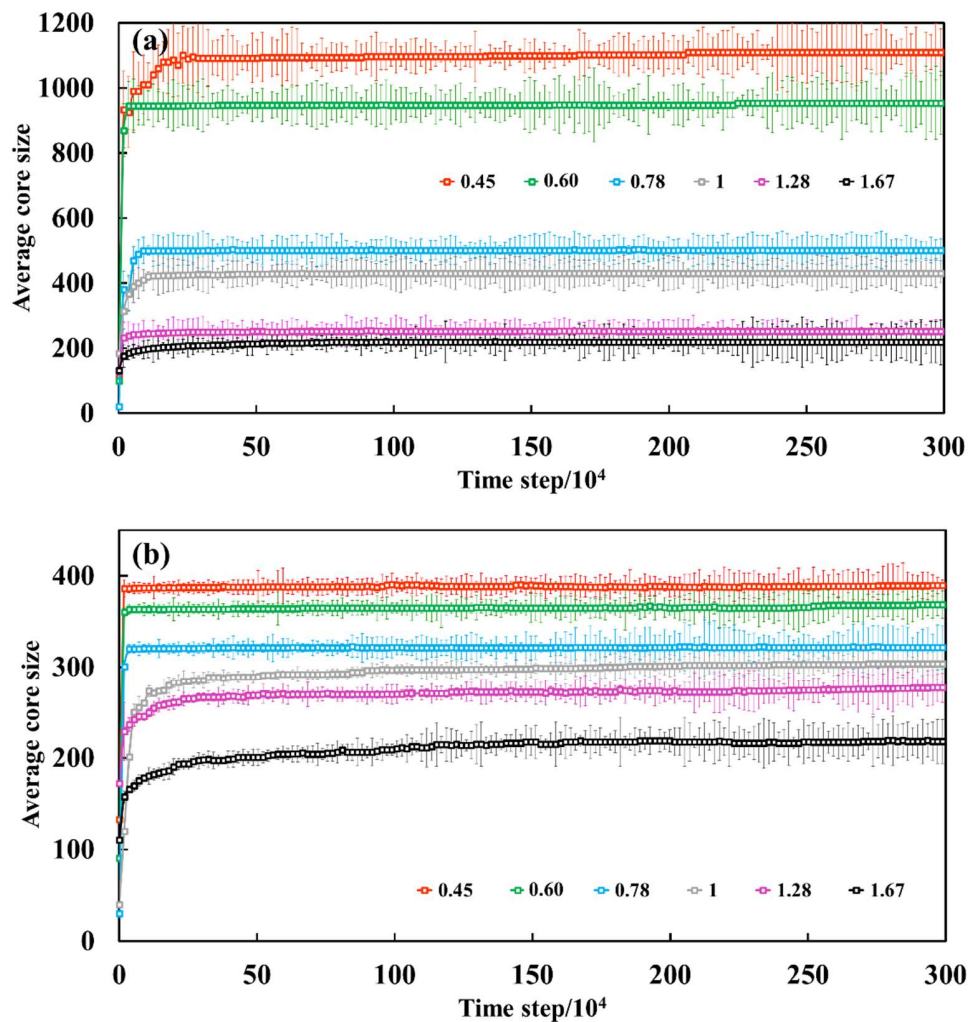


Figure S5. Time evolution of complex-core size (number of beads A in the core) for the systems with different r_b (0.45, 0.67, 0.78, 1.00, 1.28, 1.67), (a) $l_t = 80$, $a_{AW} = 40$, and $\varphi_p = 0.05$, and (b) $l_t = 80$, $a_{AW} = 40$, and $\varphi_p = 0.04$. The results were averaged together across the three simulation runs, and the standard deviations in these amounts were calculated accordingly. In the legend, the values are r_b .

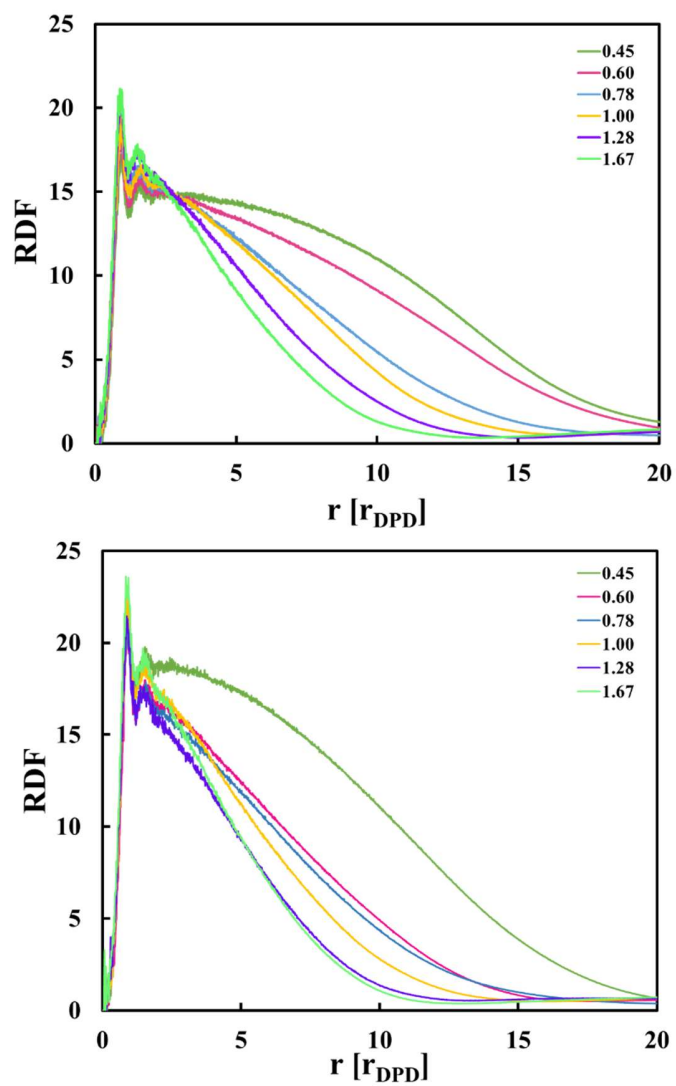


Figure S6. Radial distribution function between the IgG1 and the polyelectrolyte block (bead type A) for the systems with different r_b (0.45, 0.60, 0.78, 1.00, 1.28, 1.67), and (a) $l_t = 80$, $\alpha_{AW} = 40$ and $\varphi_p = 0.05$, and (b) $l_t = 80$, $\alpha_{AW} = 40$ and $\varphi_p = 0.04$. RDF data analysis is based on the last 20 frames of the simulations. In the legend, the values are r_b .

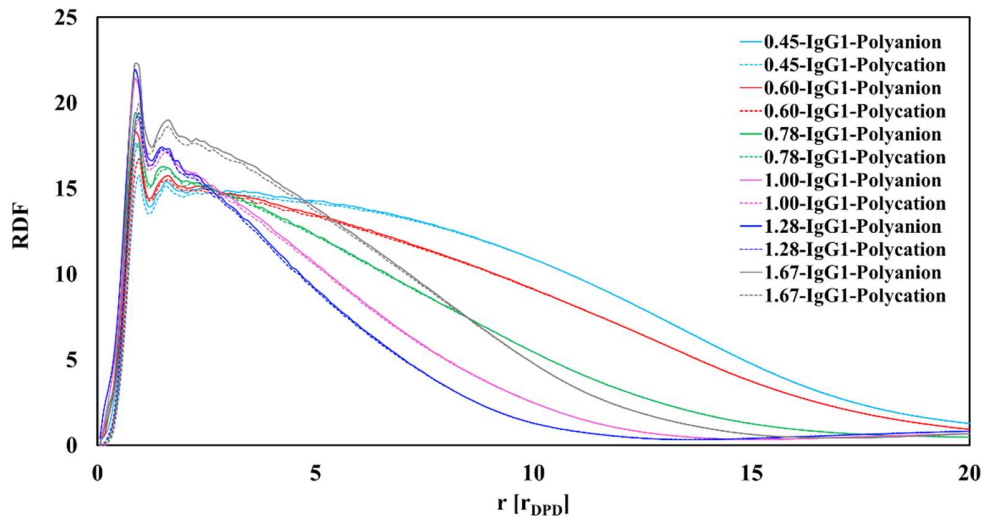


Figure S7. Radial distribution function between the IgG1 and the polyanion (and polycation) (bead type A) for the systems with different r_b (0.45, 0.60, 0.78, 1.00, 1.28, and 1.67), and (a) $l_t = 80$, $a_{AW} = 40$ and $\varphi_p = 0.05$. RDF data analysis is based on the last 20 frames of the simulations. In the legend, the values are r_b .

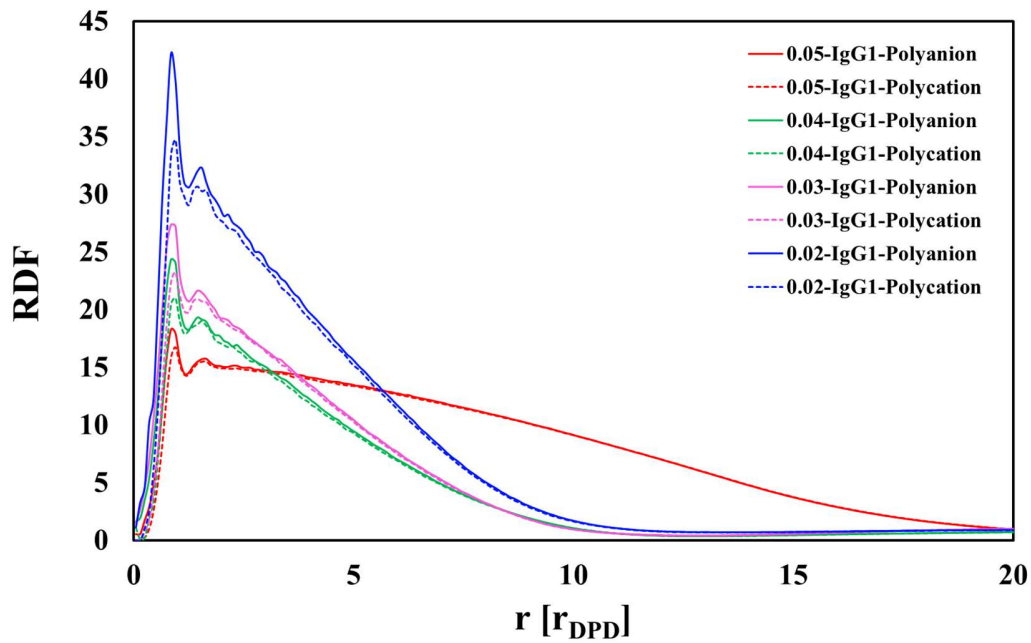


Figure S8. Radial distribution function between the IgG1 and the polyanion (and polycation) (bead type A) for the systems with different φ_p (0.02, 0.03, 0.04, and 0.05), and (a) $l_t = 80$, $a_{AW} = 40$ and $r_b = 0.60$. RDF data analysis is based on the last 20 frames of the simulations. In the legend, the values are φ_p .

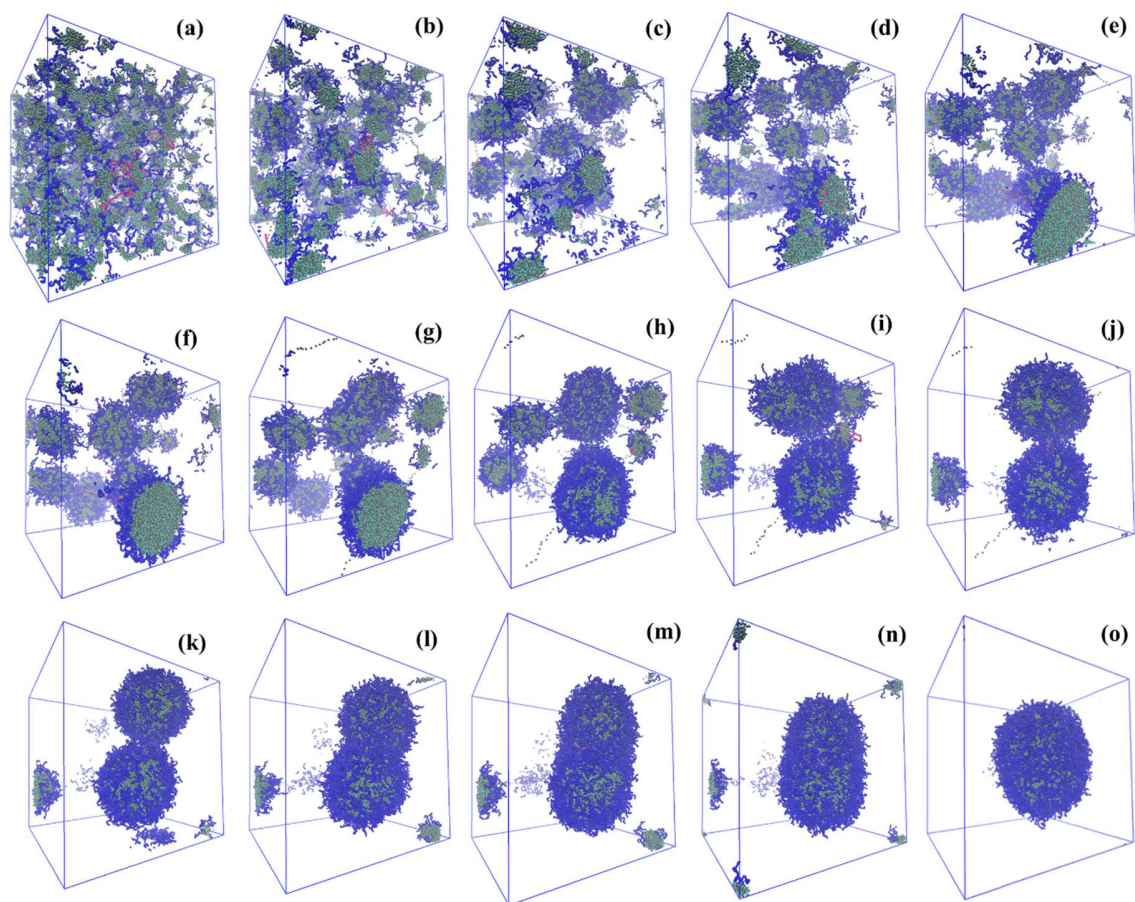


Figure S9. Time evolution of the aggregate formation and the final assembly morphology in the system consisting of IgG1, $A_{55}^+B_{25}$ and $A_{55}^-B_{25}$ ($l_t = 80, r_b = 0.45, \varphi_p = 0.05, a_{AW} = 35$). The snapshots correspond to simulation times **(a)** 6×10^3 , **(b)** 3×10^4 , **(c)** 9×10^4 , **(d)** 1.5×10^5 , **(e)** 1.8×10^5 , **(f)** 2.4×10^5 , **(g)** 3.0×10^5 , **(h)** 3.6×10^5 , **(i)** 5.1×10^5 , **(j)** 5.7×10^5 , **(k)** 7.8×10^5 , **(l)** 9.0×10^5 , **(m)** 9.3×10^5 , **(n)** 1.02×10^6 , and **(o)** 3.0×10^6 . Gray, cyan, blue and magenta beads represent A^- , A^+ , PEG, and IgG, respectively. Solvent and counterions are omitted in the visualizations for clarity.

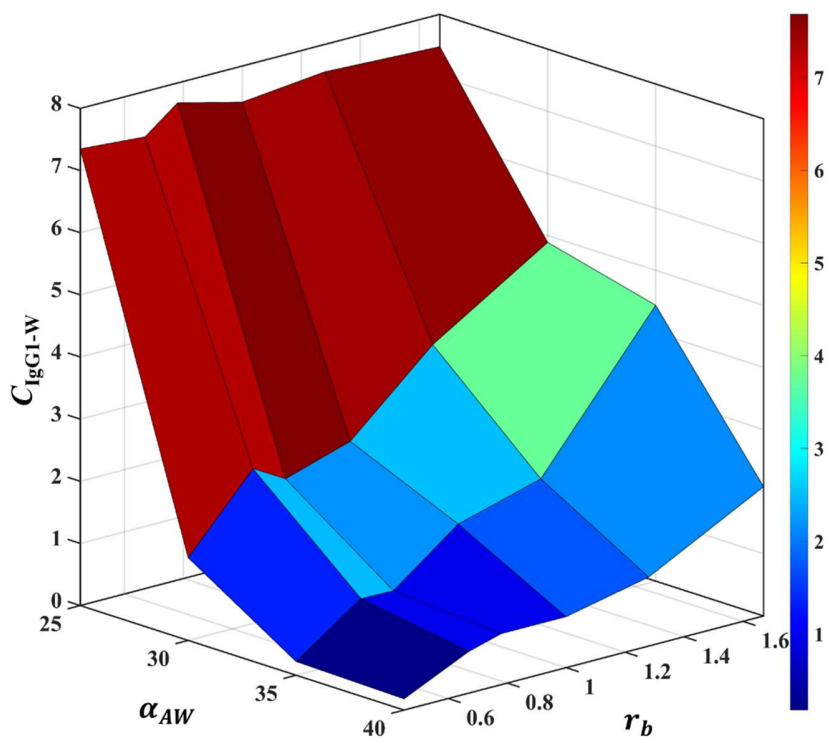


Figure S10. Average contact between IgG1 beads and water beads as a function of r_b and α_{AW} at a fixed polymer concentration $\varphi_p = 0.05$ and a fixed chain length $l_t = 80$.

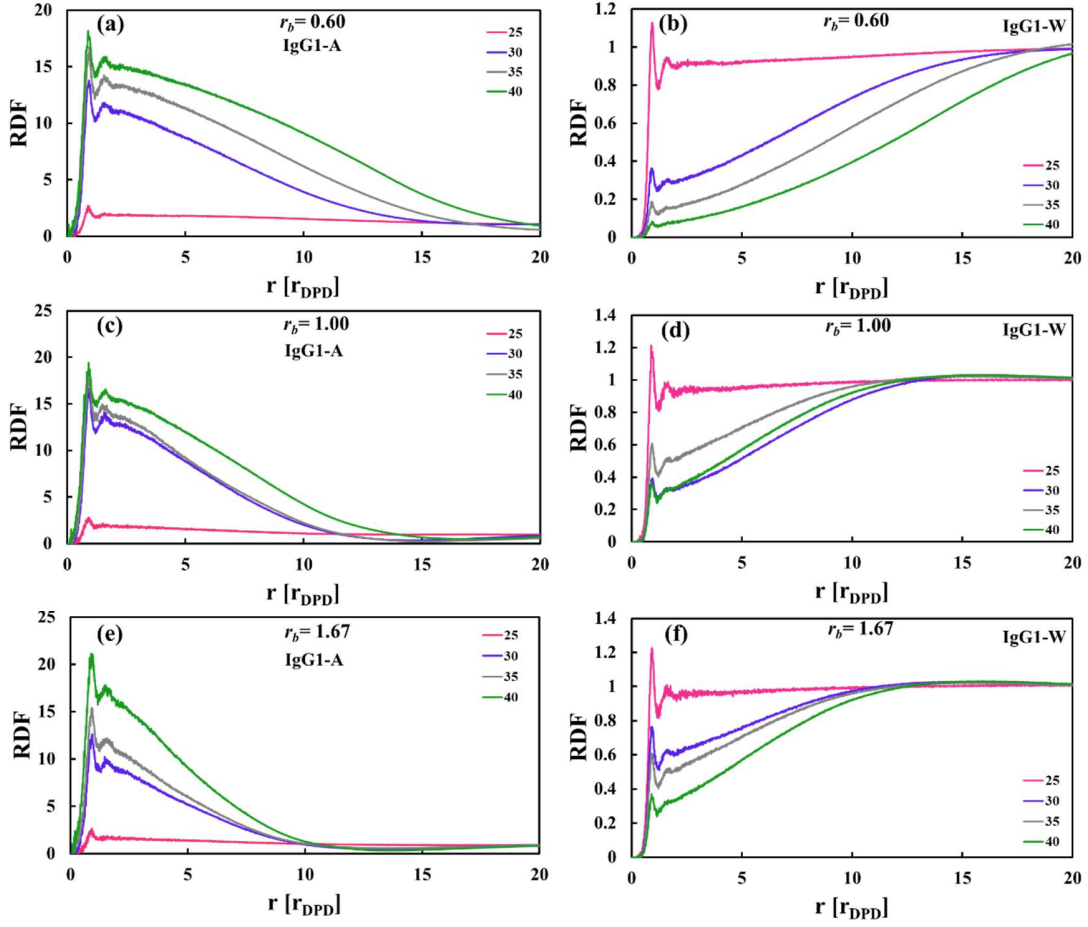


Figure S11. Radial distribution function between the IgG1 and the polyelectrolyte beads (type A) for the systems with different a_{AW} (25, 30, 35, 40), $l_t = 80$, $\varphi_p = 0.05$, and (a) $r_b = 0.60$, (c) $r_b = 1.00$, and (e) $r_b = 1.67$. Radial distribution function between the IgG1 and water for the systems with different a_{AW} (25, 30, 35, 40), $l_t = 80$, $\varphi_p = 0.05$, and (b) $r_b = 0.60$, (d) $r_b = 1.00$, and (f) $r_b = 1.67$. RDF data analysis is based on the last 20 frames of the simulations. In the legend, the values are a_{AW} .

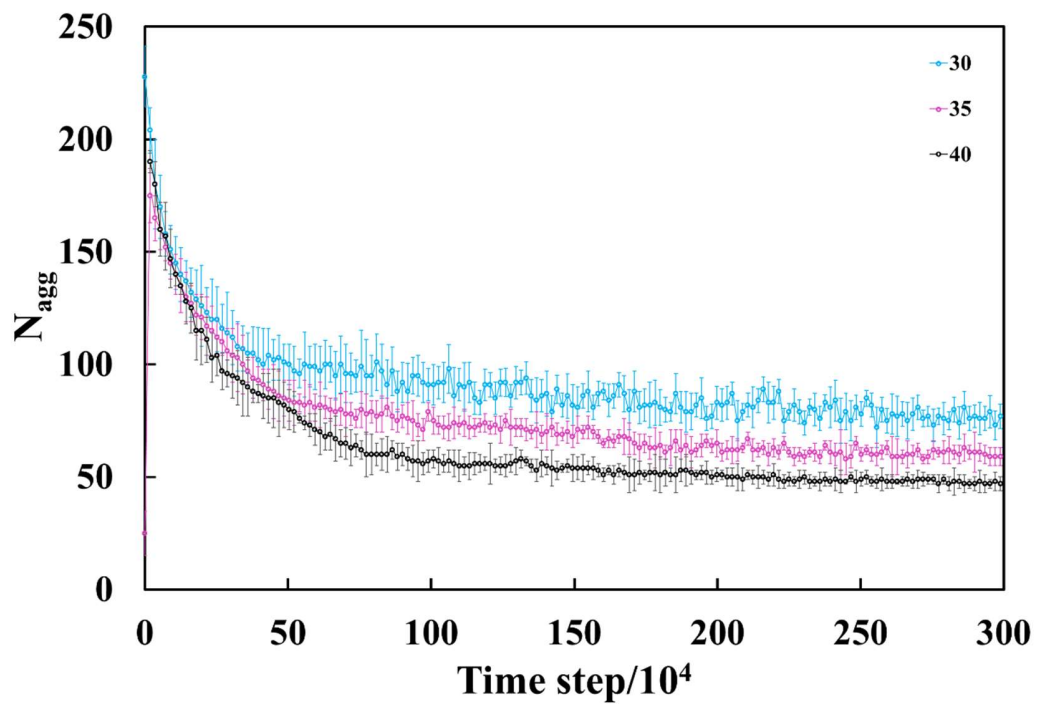


Figure S12. The time evolution of the number of aggregates (N_{agg}) at different simulation steps for different a_{AW} at a fixed polymer concentration of $\varphi_p = 0.05$, $l_t = 80$, and $r_b = 0.78$. The results were averaged across three simulation runs, with standard deviations shown as error bars. In the legend, the values are a_{AW} .

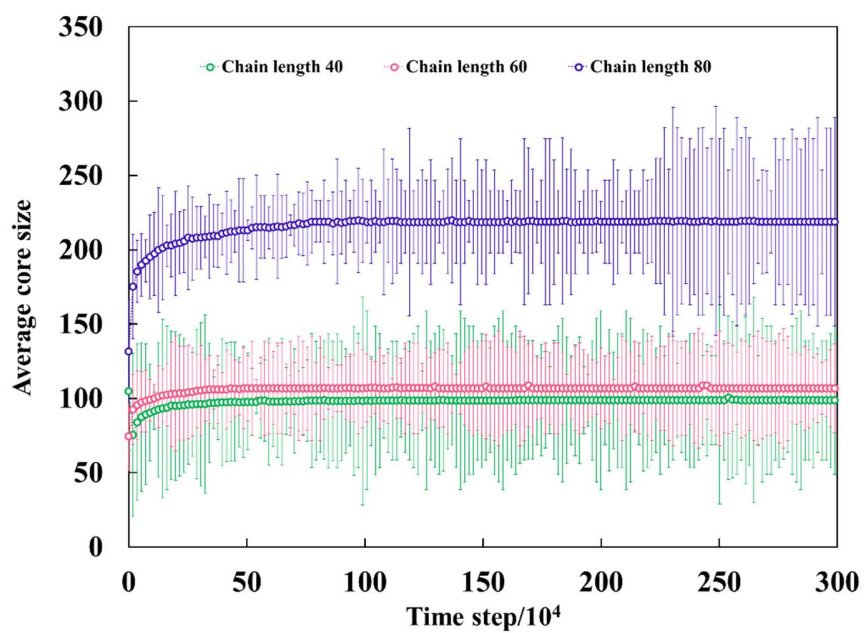


Figure S13. Time evolution of complex-core size (number of A beads in the core) for the systems with different l_t ($a_{AW} = 40$, $\varphi_p = 0.05$, $r_b = 1.67$). The results were averaged together across the three simulation runs, and the standard deviations in these amounts were calculated accordingly.

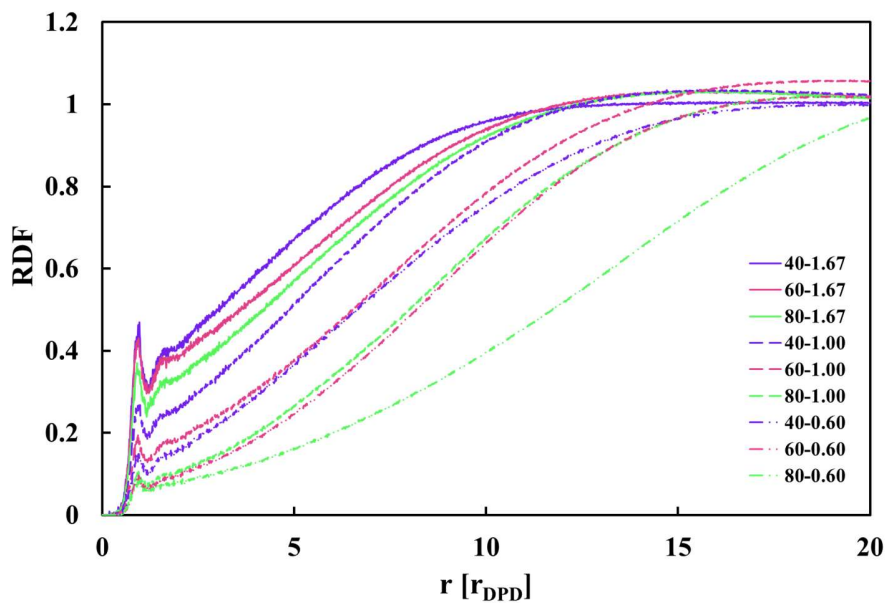


Figure S14. Radial distribution function between the IgG1 and water beads for the systems with $a_{AW} = 40$, $\varphi_p = 0.05$, as a function of l_t and r_b . In the legend, the first values are l_t and the second ones are r_b .

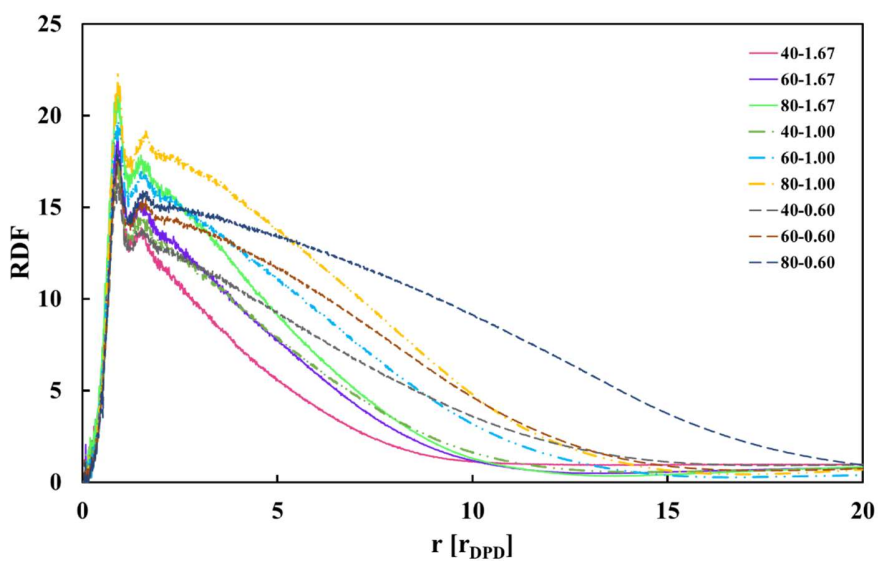


Figure S15. Radial distribution function between the IgG1 and the polyelectrolyte (bead type A) beads for the systems with $a_{AW} = 40$, $\varphi_p = 0.05$, as a function of l_t and r_b . RDF data analysis is based on the last 20 frames of the simulations. In the legend, the first value is l_t and the second is r_b .

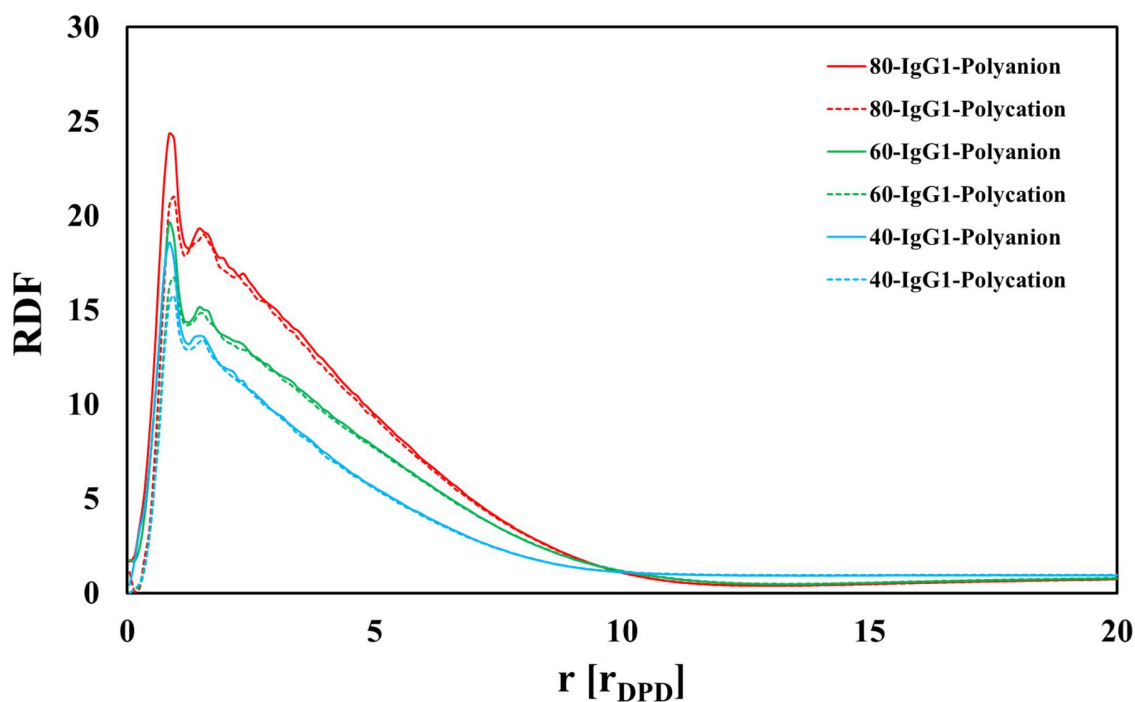


Figure S16. Radial distribution function between the IgG1 and the polyanion (and polycation) (bead type A) for the systems with different l_t (40, 60, and 80), and (a) $r_b = 0.60$, $a_{AW} = 40$ and $\varphi_p = 0.05$. RDF data analysis is based on the last 20 frames of the simulations. In the legend, the values are l_t .

References

- (1) Xie, J.; Gonzalez-Carter, D.; Tockary, T. A.; Nakamura, N.; Xue, Y.; Nakakido, M.; Akiba, H.; Dirisala, A.; Liu, X.; Toh, K.; Yang, T.; Wang, Z.; Fukushima, S.; Li, J.; Quader, S.; Tsumoto, K.; Yokota, T.; Anraku, Y.; Kataoka, K. Dual-Sensitive Nanomicelles Enhancing Systemic Delivery of Therapeutically Active Antibodies Specifically into the Brain. *ACS Nano* **2020**, *14* (6), 6729–6742. <https://doi.org/10.1021/acsnano.9b09991>.
- (2) Min, H. S.; Kim, H. J.; Naito, M.; Ogura, S.; Toh, K.; Hayashi, K.; Kim, B. S.; Fukushima, S.; Anraku, Y.; Miyata, K.; Kataoka, K. Systemic Brain Delivery of Antisense Oligonucleotides across the Blood–Brain Barrier with a Glucose-Coated Polymeric Nanocarrier. *Angew. Chem. Int. Ed.* **2020**, *59* (21), 8173–8180. <https://doi.org/10.1002/anie.201914751>.
- (3) Li, X.; Lu, C.; Xia, W.; Quan, G.; Huang, Y.; Bai, X.; Yu, F.; Xu, Q.; Qin, W.; Liu, D.; Pan, X. Poly(L-Glutamic Acid)-Based Brush Copolymers: Fabrication, Self-Assembly, and Evaluation as Efficient Nanocarriers for Cationic Protein Drug Delivery. *AAPS PharmSciTech* **2020**, *21* (3), 78. <https://doi.org/10.1208/s12249-020-1624-4>.
- (4) Nukolova, N. V.; Yang, Z.; Kim, J. O.; Kabanov, A. V.; Bronich, T. K. Polyelectrolyte Nanogels Decorated with Monoclonal Antibody for Targeted Drug Delivery. *React. Funct. Polym.* **2011**, *71* (3), 315–323. <https://doi.org/10.1016/j.reactfunctpolym.2010.10.011>.

- (5) Kim, A.; Miura, Y.; Ishii, T.; Mutaf, O. F.; Nishiyama, N.; Cabral, H.; Kataoka, K. Intracellular Delivery of Charge-Converted Monoclonal Antibodies by Combinatorial Design of Block/Homo Polyion Complex Micelles. *Biomacromolecules* **2016**, *17* (2), 446–453. <https://doi.org/10.1021/acs.biomac.5b01335>.
- (6) Pispas, S. Complexes of Lysozyme with Sodium (Sulfamate-Carboxylate)Isoprene/Ethylene Oxide Double Hydrophilic Block Copolymers. *J. Polym. Sci. Part Polym. Chem.* **2007**, *45* (3), 509–520. <https://doi.org/10.1002/pola.21871>.
- (7) Gao, G.; Yan, Y.; Pispas, S.; Yao, P. Sustained and Extended Release with Structural and Activity Recovery of Lysozyme from Complexes with Sodium (Sulfamate Carboxylate) Isoprene/Ethylene Oxide Block Copolymer. *Macromol. Biosci.* **2010**, *10* (2), 139–146. <https://doi.org/10.1002/mabi.200900186>.
- (8) Horn, J. M.; Kapelner, R. A.; Obermeyer, A. C. Macro- and Microphase Separated Protein-Polyelectrolyte Complexes: Design Parameters and Current Progress. *Polymers* **2019**, *11* (4), 578. <https://doi.org/10.3390/polym11040578>.
- (9) Nolles, A.; Hooiveld, E.; Westphal, A. H.; van Berkel, W. J. H.; Kleijn, J. M.; Borst, J. W. FRET Reveals the Formation and Exchange Dynamics of Protein-Containing Complex Coacervate Core Micelles. *Langmuir* **2018**, *34* (40), 12083–12092. <https://doi.org/10.1021/acs.langmuir.8b01272>.
- (10) Zhang, Y.; Han, K.; Lu, D.; Liu, Z. Reversible Encapsulation of Lysozyme within MPEG- b -PMAA: Experimental Observation and Molecular Dynamics Simulation. *Soft Matter* **2013**, *9* (36), 8723–8729. <https://doi.org/10.1039/C3SM50586C>.
- (11) Groot, R. D.; Warren, P. B. Dissipative Particle Dynamics: Bridging the Gap between Atomistic and Mesoscopic Simulation. *J. Chem. Phys.* **1997**, *107* (11), 4423–4435. <https://doi.org/10.1063/1.474784>.
- (12) Hoogerbrugge, P. J.; Koelman, J. M. V. A. Simulating Microscopic Hydrodynamic Phenomena with Dissipative Particle Dynamics. *Europhys. Lett. EPL* **1992**, *19* (3), 155–160. <https://doi.org/10.1209/0295-5075/19/3/001>.
- (13) Groot, R. D. Electrostatic Interactions in Dissipative Particle Dynamics—Simulation of Polyelectrolytes and Anionic Surfactants. *J. Chem. Phys.* **2003**, *118* (24), 11265–11277. <https://doi.org/10.1063/1.1574800>.
- (14) González-Melchor, M.; Mayoral, E.; Velázquez, M. E.; Alejandre, J. Electrostatic Interactions in Dissipative Particle Dynamics Using the Ewald Sums. *J. Chem. Phys.* **2006**, *125* (22), 224107. <https://doi.org/10.1063/1.2400223>.
- (15) Šindelka, K.; Limpouchová, Z.; Lísal, M.; Procházka, K. Dissipative Particle Dynamics Study of Electrostatic Self-Assembly in Aqueous Mixtures of Copolymers Containing One Neutral Water-Soluble Block and One Either Positively or Negatively Charged Polyelectrolyte Block. *Macromolecules* **2014**, *47* (17), 6121–6134. <https://doi.org/10.1021/ma501018x>.
- (16) Dandekar, R.; Ardekani, A. M. Monoclonal Antibody Aggregation near Silicone Oil–Water Interfaces. *Langmuir* **2021**, *37* (4), 1386–1398. <https://doi.org/10.1021/acs.langmuir.0c02785>.
- (17) Chaudhri, A.; Zarraga, I. E.; Kamerzell, T. J.; Brandt, J. P.; Patapoff, T. W.; Shire, S. J.; Voth, G. A. Coarse-Grained Modeling of the Self-Association of Therapeutic Monoclonal Antibodies. *J. Phys. Chem. B* **2012**, *116* (28), 8045–8057. <https://doi.org/10.1021/jp301140u>.

- (18) Shen, Z.; Ye, H.; Kröger, M.; Li, Y. Aggregation of Polyethylene Glycol Polymers Suppresses Receptor-Mediated Endocytosis of PEGylated Liposomes. *Nanoscale* **2018**, *10* (9), 4545–4560. <https://doi.org/10.1039/C7NR09011K>.